

See discussions, stats, and author profiles for this publication at: <https://www.researchgate.net/publication/275154507>

Effect of Nanoporous Gold Thin Film Morphology on Electrochemical DNA Sensing

ARTICLE in ANALYTICAL CHEMISTRY · APRIL 2015

Impact Factor: 5.64 · DOI: 10.1021/acs.analchem.5b00846

CITATIONS

6

READS

78

3 AUTHORS:



Pallavi Daggumati

University of California, Davis

9 PUBLICATIONS 42 CITATIONS

SEE PROFILE



Zimple Matharu

University of California, Davis

27 PUBLICATIONS 406 CITATIONS

SEE PROFILE



Erkin Seker

University of California, Davis

57 PUBLICATIONS 450 CITATIONS

SEE PROFILE

Effect of Nanoporous Gold Thin Film Morphology on Electrochemical DNA Sensing

Pallavi Daggumati, Zimple Matharu, and Erkin Seker

Anal. Chem., **Just Accepted Manuscript** • Publication Date (Web): 19 Apr 2015

Downloaded from <http://pubs.acs.org> on April 19, 2015

Just Accepted

"Just Accepted" manuscripts have been peer-reviewed and accepted for publication. They are posted online prior to technical editing, formatting for publication and author proofing. The American Chemical Society provides "Just Accepted" as a free service to the research community to expedite the dissemination of scientific material as soon as possible after acceptance. "Just Accepted" manuscripts appear in full in PDF format accompanied by an HTML abstract. "Just Accepted" manuscripts have been fully peer reviewed, but should not be considered the official version of record. They are accessible to all readers and citable by the Digital Object Identifier (DOI®). "Just Accepted" is an optional service offered to authors. Therefore, the "Just Accepted" Web site may not include all articles that will be published in the journal. After a manuscript is technically edited and formatted, it will be removed from the "Just Accepted" Web site and published as an ASAP article. Note that technical editing may introduce minor changes to the manuscript text and/or graphics which could affect content, and all legal disclaimers and ethical guidelines that apply to the journal pertain. ACS cannot be held responsible for errors or consequences arising from the use of information contained in these "Just Accepted" manuscripts.



ACS Publications
High quality. High impact.

Effect of Nanoporous Gold Thin Film Morphology on Electrochemical DNA Sensing

Pallavi Daggumati, Zimple Matharu, Erkin Seker*

Department of Electrical Engineering, University of California, Davis, CA, 95616

*Corresponding author: eseker@ucdavis.edu

ABSTRACT: Advances in materials science and chemistry have led to the development of a wide range of nanostructured materials for building novel electrochemical biosensors. A systematic understanding of the challenges related to electrode morphology involved in designing such sensors is essential for developing effective biosensing tools. In this study, we use nanoporous gold (np-Au) thin film electrode coatings with sub-micron thicknesses, as a model system to investigate the influence of nanostructuring on DNA–methylene blue (MB) interactions and their application for DNA biosensors. The interaction of single- and double-stranded DNA immobilized onto morphologically different np-Au films with MB was electrochemically interrogated via square wave voltammetry (SWV). The electrochemical signal from these electrodes in response to MB decayed progressively with each SWV scan. The decay rate was governed by accessibility of the electrochemically-active np-Au surface by the analyte. The optimum frequency for extracting the maximum signal via SWV was influenced by the film morphology, where the optimum frequency was lower for the nanoporous morphology with lower density of molecular access points into the porous coating. Overall, the np-Au electrodes exhibited a 10-fold enhancement in probe grafting density and approximately 10-fold higher electrochemical current upon probe-target hybridization as compared to the planar Au electrodes. The np-Au electrodes enabled sensitive detection with a dynamic range of 10 nM to 100 nM that shifts by an order of magnitude for coarsened np-Au morphology due to increased target penetration into the porous network and hence enhanced hybridization efficiency. These findings provide insight into the influence of nanostructuring on the transport mechanisms of small molecules and nucleic acids, and yield an understanding of diverse sensor performance parameters such as DNA grafting density, hybridization efficiency, sensitivity and dynamic range.

INTRODUCTION

The rapid detection of biomolecular markers is required for diagnosis, management of diseases and for conducting fundamental biological studies^{1,2}. To address this need, sensor technologies with a wide-range of detection modalities, including optical, mechanical, magnetic, and electrochemical, have been devised^{3,4}. The detection systems commonly need to be fast, accurate, and sensitive. It is also desirable to have a platform that can be easily interfaced with electronics for scale-up and multiplexed biomarker detection. To that end, electrochemical biosensors have attracted significant attention as powerful bioanalytical tools⁵⁻⁷, in particular for nucleic acid detection. Electrochemical DNA sensors have traditionally employed planar Au electrodes⁸, which offered limited sensitivity, selectivity, and limit of detection due to crowding of capture probes on the surface that limits their accessibility by target molecules⁹. Recently, nanostructuring of the electrode surface greatly mitigated these issues and enabled significant enhancement in sensor performance^{10, 11}. These enhancements include increased surface area-to-volume ratio and surface coverage of capture probes, favorable orientation of the immobilized probes, and higher electro-catalytic activity at the surface. Some of the nanostructured sensors include, carbon nanotubes^{12, 13}, gold nanopillars¹⁰, nanoporous platinum^{14, 15}, palladium and platinum clusters¹⁶. While there are numerous claims on nanostructured materials enhancing sensor performance, a systematic study as to how nanostructure enables this and what are the parameters for optimizing performance is still lacking. In order to

systematically investigate the response of DNA functionalized electrodes and the effect of nanostructure in tuning their properties, nanoporous gold (np-Au) was chosen as the model system in the current studies. Np-Au is a promising nanostructured material for developing affinity based nucleic acid sensors owing to its amenable characteristics such as high electrical conductivity^{17,18,19,20}, tunable pore morphology²¹, corrosion resistance²², biocompatibility²¹, biofouling resistance²³ compatibility with microfabrication processes^{24, 25}, and well-studied gold-thiol surface chemistry for conjugating biomolecules²⁶⁻²⁹. Np-Au is produced by a nano-scale self-assembly process, where silver atoms are dissolved from a silver-rich gold alloy in nitric acid and gold atoms diffuse at the metal-electrolyte interface to create a bicontinuous open-pore structure³⁰.

The selection of redox molecules is also crucial to fully register the electrochemical behavior of the nanostructured sensor and has a great impact on its performance. Various redox molecules such as potassium ferrocyanide, ruthenium hexamine chloride^{1, 10, 15} and methylene blue (MB)³¹⁻³⁷ have been used in the past to explore the electrochemical properties of the nanostructured materials and their utilization for nucleic acid sensing. Electrochemical reactions involving potassium ferrocyanide and ruthenium hexamine chloride are diffusion-limited due to fast electron transfer rate constant of these molecules^{38, 39}. In such cases, the redox molecule does not have enough time to permeate the high aspect-ratio nanostructures (e.g., nanopores) and thus enhanced surface area is no longer an advantage. On the other hand,

electrochemistry of MB is a combination of diffusion and surface controlled processes with the latter being dominant in DNA-functionalized electrodes⁴⁰. Consequently, a larger portion of the nanostructured surface participates in active electron transfer, thereby taking advantage of the enhanced surface area for electrochemical reactions necessary for bio-detection. Due to this, we chose MB as the model hybridization marker in the current studies and presented a systematic electrochemical analysis of the interactions of this redox marker with DNA modified np-Au films with varying morphologies. Another reason for selection of MB is its ability to differentiate between ssDNA and dsDNA. MB is known to specifically bind with ssDNA via ionic interactions and affinity binding with free guanine bases³² that decreases upon target hybridization³¹⁻³⁷. Despite successful utilization of MB as an electro-active indicator for DNA hybridization in the past, a fundamental study investigating the interactions of MB with DNA functionalized nanostructured films and influence of varying morphologies on the electrochemical properties is missing.

Here we report a comprehensive study to understand the response of MB towards DNA functionalized np-Au films and its molecular transport limitations. In addition, we investigated the impact of electrode morphology on optimal SWV frequency which is crucial for sensor response. We further demonstrated a DNA sensor by tuning the probe grafting density and dynamic range of detection by varying the extent of nanostructuring.

EXPERIMENTAL SECTION

Chemicals and Reagents

0.15 mm-thick glass coverslips (22 mm × 22 mm), used as substrates for film deposition, were purchased from Electron Microscopy Sciences. Gold, silver and chrome targets (99.95% pure) were obtained from Kurt J. Lesker. Nitric acid (70%, used as received) and MB were purchased from Sigma-Aldrich, USA. Sulfuric acid (96%) and hydrogen peroxide (30%) were obtained from J. T. Baker. Piranha solution, for cleaning glass coverslips, consisted of 1:4 ratio (by volume) of hydrogen peroxide and sulfuric acid. CAUTION: *Piranha solution and nitric acid are highly corrosive and reactive with organic materials and must be handled with extreme care.* Tris (2-chloroethyl) phosphate (TCEP), magnesium chloride, sodium phosphate monobasic, sodium phosphate dibasic were obtained from Fisher Scientific. Phosphate buffered saline (PBS) was purchased from Life Technologies. Methylene blue, carboxylic acid, succinimidyl ester (MB-NHS) were obtained from Biosearch Technologies. The oligonucleotides used in this project consisted of 26 bases and were purchased from Integrated DNA Technologies, USA. The 5' end of probe ssDNA (p1 and p2) was modified with a C6 linker and thiol group. 3' end of p2 was modified with an amine group to enable tagging with MB.

Probe ssDNA (p1): 5ThioMC6-D/CGT GTT ATA AAA TGT AAT TTG GAA TT;

Probe ssDNA (p2): 5ThioMC6-D/CGT GTT ATA AAA TGT AAT TTG GAA TT/3AmMO

Target DNA (t1): AAT TCC AAA TTA CAT TTT ATA ACA CG

Fabrication of nanoporous gold (np-Au) electrodes

Np-Au gold films were prepared as described previously⁴¹. Briefly, the glass coverslips were cleaned by immersion in a

freshly-prepared piranha solution for 10 minutes, rinsed with deionized (DI) water, and dried under nitrogen flow prior to metal deposition. First, a 160 nm-thick chrome layer was sputtered to promote adhesion between the glass substrate and the subsequent metallic layers. Next, 80 nm-thick seed layer of gold was sputtered and finally silver and gold were co-sputtered from different targets to obtain 600 nm thick alloy layer. All depositions were performed in argon at a pressure of 10 mTorr. The samples were then dealloyed in 70% nitric acid at 55 °C for 15 minutes to produce the np-Au films and then rinsed with DI water. In order to obtain samples with different pore morphology (annealed np-Au), a group of dealloyed samples were thermally treated for 3.5 minutes at 225 °C on a hot plate. Planar gold electrodes were also fabricated by sputter-depositing a 50 nm-thick chrome adhesion layer followed by 250 nm-thick gold film onto piranha-cleaned glass cover slips.

Characterization of np-Au morphology

Top and cross-sectional views of the samples with different morphologies were captured with a scanning electron microscope (FEI Nova NanoSEM430) at 100 kX magnification to investigate micro- and nano-scale morphological features, as well as the thickness of np-Au films. Top-view images of samples were analyzed using ImageJ (National Institutes of Health shareware, <http://rsb.info.nih.gov/ij/index.html>) in order to determine the average pore and ligament sizes for various morphologies. Briefly, the grayscale SEM images were segmented into monochrome images and threshold was adjusted in order to define pores as black and ligaments as white. Crack and pore areas as well as perimeters were extracted from these processed images to be used as metrics for evaluating biomolecule access into the porous coating.

Immobilization of probe DNA on electrodes

Thiolated probe DNA stock solution was reduced in 5 mM TCEP solution for 2 h and excess TCEP was filtered out. TCEP provided higher yield of reduced DNA and a simpler filtration protocol in comparison to reagents such as DTT⁴². For immobilization, the electrodes were first cleaned in dilute (1:4) piranha solution for 20 seconds. These electrodes were then incubated in an immobilization solution containing 25 mM phosphate buffer (PB), 2 μM thiolated probe DNA (p1) and 50 mM MgCl₂ for 1.5 h at room temperature. The probe-modified electrodes were further treated with a back-fill agent, 1 mM mercaptohexanol (MCH) prepared in PB for 2 h to obtain a well-ordered DNA-MCH monolayer. The electrodes were thoroughly rinsed with PB to remove non-specifically bound DNA. To investigate DNA-MB interaction mechanism, DNA functionalized electrodes were incubated in 150 μl of 20 μM MB prepared in 1X PBS for 10 minutes. The electrodes were washed after MB accumulation to remove unbound MB molecules. Subsequently, the electrode was placed inside a custom-built Teflon electrochemical cell and 1X PBS buffer was used for subsequent electrochemical measurements. For control measurements, covalently conjugated MB-DNA was employed. For this, amine modified 26mer probes (p2) were tagged with MB via a previously reported method⁴³. Thiol reduction and immobilization of these probes was carried out in a similar way as the untagged probes.

Hybridization of target DNA

Probe modified electrode was challenged with different concentrations of target DNA. The electrode was incubated with desired target DNA prepared in PB containing 50 mM MgCl₂ for 35 minutes at 37 °C. The electrode was then rinsed to remove non-specifically bound target molecules. MB accumulation was again performed in a similar manner.

Electrochemical characterization

All electrochemical measurements were performed in a homemade Teflon cell integrated with a Gamry Reference 600 potentiostat. Np-Au or planar Au electrodes having a foot print of 0.15 cm² were used as working electrodes. Platinum wire and Ag/AgCl electrodes were used as counter and reference electrodes, respectively. Cyclic voltammetric (CV) measurements were performed in 0.05 M sulfuric acid at a scan rate of 50 mV/s over the potential range, -0.25 mV to 1.75 mV to determine the effective surface area of the np-Au and planar Au electrodes. Square wave voltammetry (SWV) was utilized to interrogate the probe grafting and target hybridization on the electrodes. SWV was carried out in 1X PBS over the potential range of 0 to -0.5 mV with an amplitude of 40 mV, step size of 4 mV, and pulse frequencies ranging from 3 Hz to 60 Hz.

RESULTS AND DISCUSSION

The goal of this paper is to understand the effect of nanostructuring on various factors that dictate performance of electrochemical DNA sensors by using np-Au as a model system. The results discussed here include: (i) morphological characterization of np-Au electrodes by SEM; (ii) characterization of effective surface area of np-Au electrodes by oxide stripping technique; (iii) response of DNA functionalized np-Au films to MB and molecular transport limitations; (iv) dependence of optimal SWV frequency on electrode morphology; and (v) demonstration of a DNA sensor by tuning the probe grafting density and dynamic range of detection by varying the extent of nanostructuring.

Morphological characterization

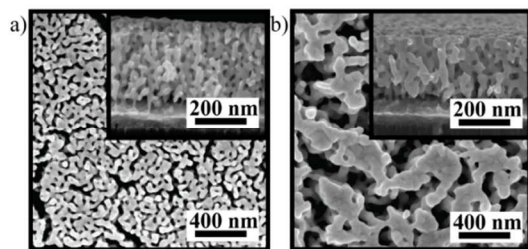


Figure 1. Scanning electron microscope images of a) un-annealed np-Au film; b) annealed np-Au film (Obtained via thermal treatment at 225 °C). Insets: Cross-sectional views.

Pores, ligaments and cracks are the key features in np-Au morphology. Typical pore size was between 20–120 nm and the morphology remained uniform through the film thickness. We noticed crack-like void formations after dealloying as shown in Figure 1a, possibly due to volume contraction during dealloying and the brittle nature of nanoporous metals⁴⁴. In order to investigate the effect of pore morphology on MB-DNA interactions, a group of np-Au samples were thermally annealed. This increases the surface diffusion of gold atoms and leads to coarsening of ligaments and expansion of cracks resulting in a different morphology of np-Au films²¹ (Figure

1b). The side walls of cracks in the annealed films offer additional surfaces for ionic transport and make the porous structure more accessible. Side wall area (additional surfaces for molecular permeation into the np-Au film) available in both morphologies was determined by multiplying the average crack perimeter by number of cracks and film thickness. The total flux area available for ionic transport was obtained by adding the side wall area to the total porous island area for each morphology. The flux area of the un-annealed np-Au films was 1.3×10^{14} nm². For annealed films, expansion of cracks resulted in 2-fold increase in the flux area. As the accessibility of the film by the analyte was largely dictated by the flux area available for the ionic transport, the annealed films were twice as accessible as the un-annealed films.

Determination of surface area by cyclic voltammetry

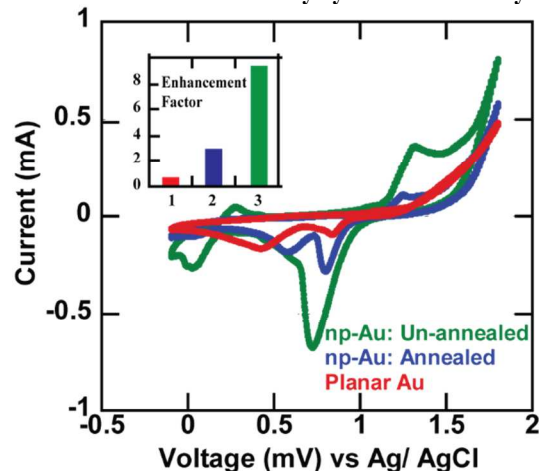


Figure 2. CV measurements of np-Au, annealed np-Au and planar Au films performed in 0.05 M sulfuric acid at a scan rate of 50 mV/s. Inset: Enhancement factors of different morphologies: 1) planar Au, 2) annealed np-Au, 3) un-annealed np-Au.

Traditional surface area measurement techniques, such as Brunauer-Emmett-Teller (BET), cannot be used for characterizing the surface area of sub-micron thin films as those techniques require a specific surface area of ~ 5 m²/g⁴⁵. Alternatively, measurement of charge required to strip the gold oxide layer via CV provides an accurate measurement of the effective area^{38, 45}. This reaction is not mass transport-limited and therefore the entire nanostructured surface participates in the reaction, enabling a reliable estimate of surface area. Figure 2 illustrates the cyclic voltammograms of planar Au and np-Au films, revealing a drastic increase in the current values for np-Au films as compared to the planar Au electrode. The electrical charge under the gold oxide reduction peak between the potentials 720 mV and 970 mV was converted into the effective surface area by using 450 μ C/cm² as the specific charge required for gold oxide reduction⁴⁵. The ratio of the effective surface areas of different np-Au samples to the effective surface area of control planar Au sample was defined as *enhancement factor*, E_h . The effective surface area of np-Au samples was 6.55 cm² displaying a significant E_h of 9.26. Thermally-annealed np-Au samples had a lower E_h , 2.41 possibly due to pore coalescence resulting in a decrease in the number of pores.

Interaction of MB with probe-modified np-Au films

In the current study, probe-functionalized np-Au films were

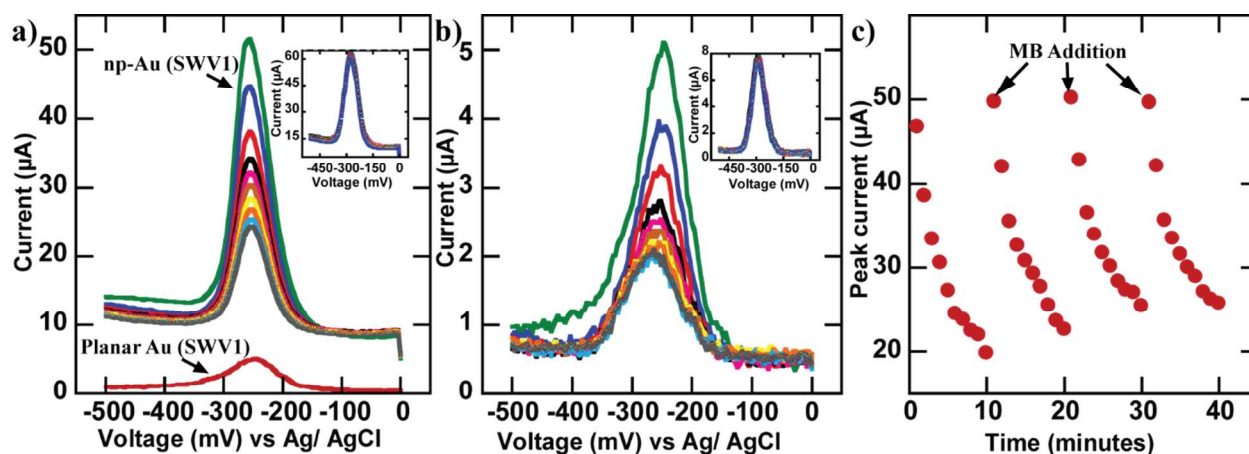


Figure 3. SWVs obtained from probe-modified electrodes in response to MB in 1X PBS. Signal decay with successive SWV scans for a) Un-annealed np-Au, b) planar Au films; Insets: SWVs scans of MB-tagged probe DNA in 1X PBS on a) un-annealed np-Au, b) planar Au films c) Signal regeneration by addition of fresh MB after every 10 SWV scans. The plot shows signal decay and regeneration upon MB replenishment in np-Au films.

characterized by SWV to study their response to MB and mass transport limitations. Un-annealed np-Au and planar Au films were functionalized with p1 probes and incubated with MB. SWV was performed at 18 Hz for np-Au and at 60 Hz for Au. The frequencies were selected by studying a range of frequencies as a function of morphology (discussed in the next section). The peak current in np-Au films was 10 times higher than planar Au as shown in Figures 3a, Figure S1, which correlates well with the increase in surface area ($E_b = 9.26$). This suggests that the entire surface is participating in the electrochemical reaction. The probe peak current was reproducible for different electrodes with an average of 43 μA and a standard deviation of 4.7 μA for $n=4$ samples. We observed a decrease in the MB peak current with successive SWV scans in both np-Au and planar Au films as shown in Figure 3a and b. The dissociation of MB from electrode surface into the electrolyte solution might be the reason for such a decrease in signal. After each SWV scan, the electrode surface is rich with reduced (less positively charged) MB molecules³⁷. These molecules are now loosely bound to the immobilized DNA molecules and tend to move away from the sensor surface into the electrolyte³⁷. As the dissociated MB molecules disperse into the electrolyte, they become dilute and cannot move towards the electrode against the concentration gradient. This effectively leads to less MB available (hence a decrease in signal amplitude) with successive scans.

Transport limitations, especially for MB to penetrate the porous structure once dispersed into the electrolyte, are more prominent in np-Au films owing to their highly tortuous structure²¹. Hence the extent of signal reduction was greater in np-Au (65%) compared to planar Au (50%). The dissociation constant of MB for planar Au was calculated to be 0.07/min (Figure S2a), which is in good agreement with the previously reported values³⁷. However, this analysis is not applicable for the np-Au films due to the complex MB dissociation phenomena involving transport of desorbed MB through the pores into the electrolyte (Figure S2b). In order to further validate the MB dissociation phenomenon leading to signal decay, a similar experiment was performed with MB covalently-attached to probe DNA. The signal was stable for over ten SWV scans with less than 5% decay as shown in the

insets of Figures 3a and b. This further confirms that transport limitations of non-covalently-bound MB molecules are responsible for the signal depletion.

The detection of DNA hybridization using MB is a signal off mechanism, that is, a decrease in the current is expected upon hybridization³¹. However, in the presence of the decaying signal with successive SWV measurements, it would be difficult, if not impossible, to differentiate the signal drop caused by a hybridization event. In order to overcome this ambiguity, MB signal needs to be regenerated before performing target hybridization. To achieve this, the MB signal was depleted by performing ten consecutive SWV scans and the probe-grafted sample was again incubated with fresh MB to instate a definite electrochemical current baseline. The initial signal could thus be regenerated multiple times by successive depletion and regeneration steps as shown in Figure 3c. The regenerated signal was within 5 % of the starting signal after each MB replenishment cycle. Hence, it is essential to first perform multiple SWV scans on the probe and deplete the signal before target hybridization. This ensures that the signal reduction is only due to the target and not due to the signal decay upon multiple scans. This technique of MB replenishment enables the same np-Au electrode to be used successively for the detecting multiple concentrations of target DNA molecules.

SWV signals as a function of frequency for different np-Au morphologies

The amplitude of the peak current is used as a metric for characterizing the bound target in case of SWV-based sensors. This signal amplitude is a function of the SWV frequency and electrode morphology. Np-Au films display high surface area that can result in signal enhancement. However, the entire surface contributes to the signal enhancement only when the electrochemical measurement is carried out at the right frequency⁴⁴. The frequency that allows the participation of the entire surface in the redox reaction relies on the rate of analyte transport in and out the nanostructured film, which in turn depends on accessibility of the entire electrode surface by constituents of the reaction (e.g., redox molecules, target DNA, ions). This section focuses on the effect of

nanostructuring on optimum frequency for obtaining the highest signal.

We examined the response of probe-functionalized np-Au films (both un-annealed and annealed) to MB at SWV frequencies in the range 3 Hz to 60 Hz (Figure 4). For planar Au electrodes, signal amplitude increased with frequency until 60 Hz and then saturated. Hence 60 Hz was chosen as the optimum frequency for sensor operation. However, in case of np-Au films, signal amplitude increased until a certain critical frequency (18 Hz and 30 Hz for un-annealed and annealed np-Au respectively) and decreased at higher frequencies as shown in Figure 4 and supplementary Figures S3a and b. Thus critical frequency for obtaining the maximum SWV amplitude depended on the morphology of the np-Au film. The flux area available for ionic transport increased in annealed np-Au films making the structure more accessible, thereby increasing the critical frequency from 18 Hz in un-annealed films to 30 Hz in annealed films. We chose these critical frequencies as the optimum frequencies for np-Au electrodes for subsequent studies.

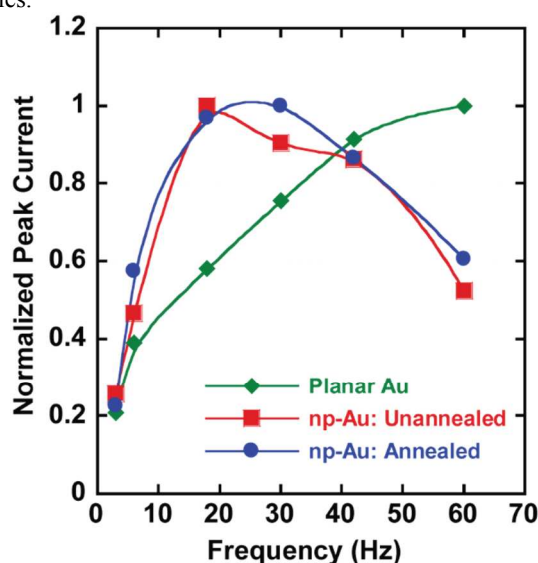


Figure 4. SWVs were obtained from probe-modified electrodes in response to MB at 3 Hz to 60 Hz. Plot shows the peak current as a function of frequency for un-annealed, annealed np-Au and planar Au. Peak current was normalized to the maximum peak current value obtained at the critical frequency for np-Au films and the saturation current value for planar Au. Curves are visual guides only.

Beyond the critical frequency, the rate of increase in faradaic current with frequency decreased in np-Au films (Figure S3c, supporting information). This decrease is attributed to the ionic species in the electrolyte not having sufficient time to fully permeate the nanoporous electrode at high frequencies, limiting the electrochemically active surface area. This result is in agreement with previous experiments demonstrating limited accessibility of the porous surface at comparable scan rates^{39, 45, 46}. In contrast, the rate of increase of SWV signal for planar Au was constant within the same frequency range (Figure S3d). A similar behavior was observed for MB-tagged probe DNA (p2) immobilized on np-Au and planar Au electrodes, despite the fact that the MB molecules were restricted from moving (Figure S4). This further confirms that

the transport of ionic species is the underlying reason for this phenomenon and not the dissociation of MB molecules.

Effect of electrode coating morphology on probe grafting density

The technique of MB regeneration and identification of optimum frequencies for different morphologies enable the development of a sensor for detecting DNA hybridization using MB as an efficient redox marker for np-Au films. Target hybridization mainly depends on the amount of probe molecules available. However, densely-packed probe layers may also give rise to electrostatic and steric hindrances for target DNA. Thus an optimum density of probe is crucial for enhanced sensor performance that can be achieved by tuning the nanostructure.

We define probe grafting density (GD) as the number of probe molecules normalized to the electrode surface area. In case of planar Au electrodes, there is an optimal GD such that it is high enough to capture low concentrations of analyte DNA and produce measurable signal changes while low enough to not cause steric hindrance for target hybridization⁴⁷. In order to study the effect of morphology in tuning GD, three sets of samples (un-annealed np-Au, annealed np-Au and planar Au films) were incubated with 26mer probe DNA (p1 and p2). MB accumulation was carried out on samples functionalized with p1 probes. This step was not required for samples functionalized with p2 probes, since MB molecules were covalently attached to the probes prior to electrode functionalization. SWV measurements were performed at optimum frequencies of 18 Hz for un-annealed np-Au, 30 Hz for annealed np-Au and 60 Hz for planar Au films. A 10-fold enhancement in peak current was obtained in un-annealed and annealed np-Au films compared to the planar Au films in both p1 and p2 probes. In case of p1 probes, each probe molecule provides sites for physical adsorption of MB. However, it is difficult to estimate the exact number of MB molecules per probe molecule. On the contrary, for the case of MB-tagged DNA (p2), each DNA molecule is covalently-labeled with a single MB molecule. Also, the DNA grafting procedure is the same for both p1 and p2 probes. Therefore, p2 probes were used for estimating GD on different morphologies of electrodes.

The total number probe molecules (N_{tot}) on the electrode surface for different morphologies were estimated from the SWV peak current using a previously described model that predicts the voltammetric peak profile of a surface redox reaction (1)^{48,49}:

$$I = \frac{2nfFN_{tot} \sinh\left(\frac{nFE}{RT}\right)}{\cosh\left(\frac{nFE}{RT}\right) + 1}$$

where I is the average peak current, n is the number of electrons ($n=2$ for MB) transferred in the redox reaction, f is the SWV frequency, F is the Faraday's constant, R is the universal gas constant, T is the temperature, and E is the peak amplitude. N_{tot} was then normalized to the electrode surface area to obtain GD.

The GDs for different electrode morphologies are summarized in Table 1. In particular, GD on planar Au electrodes was comparable to those calculated in literature via electrochemistry⁴⁷ and fluorescence⁵⁰, which validated our method of estimating GD. These densities also matched

closely with those obtained from probes with physically adsorbed MB analyzed in a similar way.

A higher GD was observed in both un-annealed and annealed np-Au films as compared to planar Au films. GD of annealed np-Au films was twice that of un-annealed films. Although the un-annealed films provide higher surface area, because of more accessibility, the number of probe molecules per unit surface area is higher in case of annealed films. It can be further hypothesized that the combination of a higher GD and enhanced accessibility may lead to better target hybridization in annealed films compared to un-annealed np-Au films.

Table 1. Comparison of probe grafting density on different electrodes.

Morphology	Grafting Density (molecules/cm ²)	Enhancement factor
Planar Au	$2.36 \pm 0.66 \times 10^{11}$	1
np-Au: Un-annealed	$6.58 \pm 0.17 \times 10^{11}$	9.26
np-Au: Annealed	$1.21 \pm 0.03 \times 10^{12}$	2.41

Target hybridization on different morphologies

In order to determine the detection range of target DNA, the probe-functionalized nanostructured sensors were challenged with different concentrations of target DNA. A decrease in the MB signal was observed after target hybridization, which is attributed to the hindrance of MB interaction due to lack of free guanine bases in dsDNA³⁰. The difference in peak current between probe and target was about 10 times higher in np-Au films compared to planar Au films as shown in Figure 5. MB was depleted via ten successive SWV cycles and replenished after obtaining probe baseline and for each of the target concentrations. Figure 5 shows the first SWV scan obtained for each target concentration and the peak current was considered for quantitative evaluation of the sensor (inset: Figure 5). The sensor exhibited a linear response between 10 nM–100 nM of target concentration (inset: Figure 5). Planar Au-electrodes did not display any change in signal strength within this concentration regime but showed a linear response at a higher concentration between 1 μ M to 10 μ M. 100 fold improvement in sensitivity and shift in dynamic range was observed with un-annealed np-Au as compared to planar Au.

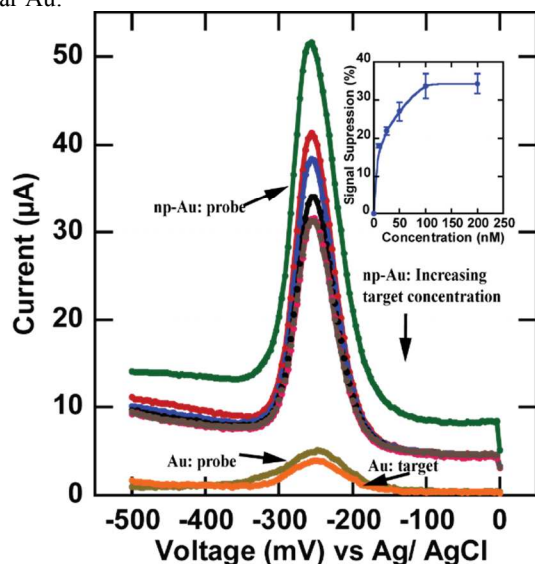


Figure 5. SWV scans of probe and target at different concentrations on np-Au electrodes and comparison with planar Au. Inset: Sensor response upon target hybridization on un-annealed np-Au electrode. Signal suppression was defined as $(I_{\text{probe}} - I_{\text{target}} / I_{\text{probe}}) \times 100$.

Increased accessibility due to larger pores in annealed films may facilitate better transport of target molecules resulting in enhanced hybridization efficiency and detection of lower concentrations of target molecules. To investigate this, annealed np-Au samples were used for target hybridization. SWV was performed at the optimum frequency (30 Hz) for these samples. It was possible to detect target concentrations as low as 500 pM with annealed np-Au films. The dynamic range of annealed np-Au films was 0.5 nM to 10 nM which was shifted by an order of magnitude compared to un-annealed np-Au films and two orders of magnitude compared to planar Au films, as shown in Figure 6.

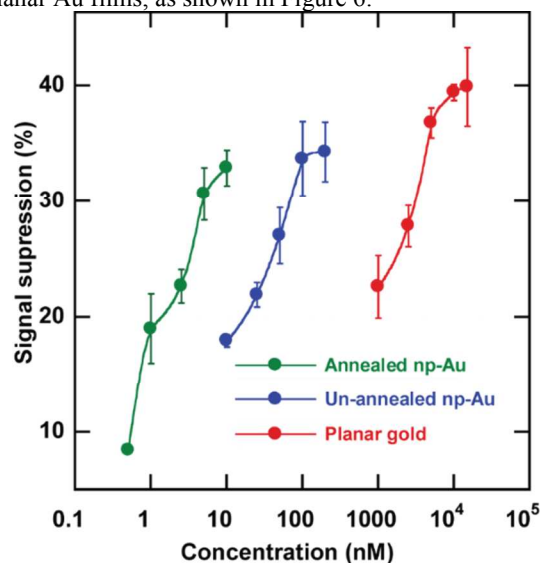
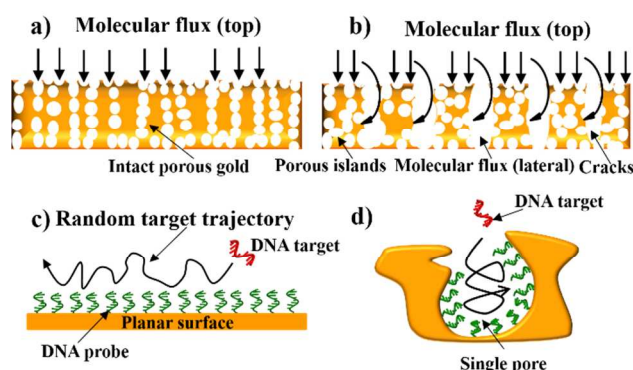


Figure 6. Shift in dynamic range of detection due to nanostructuring.

The hybridization event in un-annealed and annealed np-Au morphologies can be viewed as a combination of two events, as illustrated in Scheme 1. Event 1 corresponds to target molecules entering the pores and Event 2 corresponds to the target molecule binding with probe molecules upon entering the pore. The factor that determines the efficiency of a target molecule entering the porous structure is geometric accessibility, that is, access points of molecules into the porous electrode. Once inside the porous structure, the probability of a target molecule binding to the probe molecule should mainly depend on the interplay of two factors (i.e., GD and orientation of probe molecules). GD of np-Au films was greater than planar Au electrodes. Consequently a target molecule encounters a significantly higher number of probe molecules within a pore compared to a planar surface, thereby significantly increasing the probability of hybridization. These two factors together, resulted in enhanced hybridization in np-Au electrodes.

The flux area (geometric surfaces where molecules can permeate the porous electrode) in annealed films is twice that of un-annealed films. This enhances the occurrence of Event

1, which is the transport of target molecule into the porous network in annealed films. The transport of target molecules to the electrode surface can be further facilitated by embedding the electrodes in shallow microfluidic channels thereby reducing transport duration within the electrolyte. Probe grafting density in annealed np-Au films is twice that of un-annealed films. Hence, there is an increase in the probability of binding of the target molecule once it is inside the pore (Event 2). These two factors together (i.e., enhanced accessibility and higher probe grafting density in annealed films) enabled the detection of lower concentrations of target molecules and resulted in a shift in dynamic range of detection. A similar tuning phenomenon was observed for dendritic electrode structures obtained by electrodeposition of palladium thin films. For this convex electrode geometry, which can be conceptualized as an inverse geometry of the largely concave np-Au geometry, the enhanced sensor performance was attributed to larger deflection angles between grafted probe molecules enabled by small radius of curvature of the electrode nanostructures^{16, 51, 52}. Finally, it should be noted that the sensor discussed in this study was not optimized for lower detection limits and it can be significantly improved by reducing electrochemical cell volume (e.g., via microfluidics) and electrode size to optimize target-to-electrode transport and reaction rates^{53, 54}.



Scheme 1. a) For the un-annealed np-Au with minimal cracks, the molecules (e.g., DNA probes) can permeate the porous films only from the top surface. b) For annealed np-Au with cracks separating the porous islands, the molecules can permeate the porous film from the top and side of the islands, thereby enhancing the accessibility of the porous electrode. c) For a planar electrode, a target DNA moving randomly through the solution has a small probability of making molecular contact, that is, hybridizing with the immobilized DNA probes. d) For a porous electrode, once the target DNA enters the pore, it is surrounded by surfaces immobilized with probe DNA and the random movement yields a much higher hybridization probability.

CONCLUSION

We demonstrated the effect of varying np-Au morphologies on the performance of an electrochemical DNA biosensor. Our studies revealed that the extent of SWV signal decay due to MB dissociation from the DNA grafted films depend on the morphology of the electrode. Additionally, an optimum SWV frequency is required to realize the benefit of the entire nanostructured surface. These concepts provided insight into DNA grafting density and hybridization efficiency on the np-Au electrodes. The np-Au sensor displayed a 100-fold shift in

dynamic range of detection towards lower concentrations of DNA as compared to its planar counterpart. Annealed np-Au films showed improved accessibility and a further 10-fold shift in dynamic range of the sensor. We have shown that engineering the nanostructure to manipulate the sensitivity of each sensing element is a powerful strategy to tune the dynamic range. These studies can further be extended to design an array of nanostructured sensing elements with varying morphologies on a single chip with each element being responsive at a different concentration regime for detecting multiple targets. The concepts presented here can also be applied to the design of DNA sensors based on other nanostructured materials. We expect this fundamental study will be a path to rationale development and implementation of nanostructured sensors for point-of-care diagnostics and medical research.

ACKNOWLEDGEMENTS

We gratefully acknowledge the support from UC Lab Fees Research Program Award (12-LR-237197), Research Investments in the Sciences & Engineering (RISE) Award, and UC Davis College of Engineering start-up funds. We also thank Prof. Josh Hihath, Dr. Juan Manuel Artes Vivancos for discussions on DNA-surface interactions and Tatiana Dorofeeva for her assistance in obtaining SEM images.

ASSOCIATED CONTENT

Supporting Information

Text and figures discussing dissociation constants of MB on planar and np-Au electrodes and SWV responses as a function of frequency for un-annealed and annealed np-Au morphologies. This material is available free of charge via the internet at <http://pubs.acs.org>

AUTHOR INFORMATION

Corresponding Author

*Phone: 530-752-7300 E-mail: eseker@ucdavis.edu.

Notes: The authors declare no competing financial interest.

REFERENCES

- Lord, H.; Kelley, S. O. *Journal of Materials Chemistry* **2009**, *19* (20), 3127-3134.
- Foudeh, A. M.; Didar, T. F.; Veres, T.; Tabrizian, M. *Lab on a Chip* **2012**, *12* (18), 3249-3266.
- Borisov, S. M.; Wolfbeis, O. S. *Chemical reviews* **2008**, *108* (2), 423-461.
- Sassolas, A.; Leca-Bouvier, B. D.; Blum, L. J., *Chemical reviews* **2008**, *108* (1), 109-139.
- Taitt, C. R.; Anderson, G. P.; Lingerfelt, B. M.; Feldstein, M. J.; Ligler, F. S. *Analytical chemistry* **2002**, *74* (23), 6114-6120.
- Wang, Y.; Dostalek, J.; Knoll, W. *Analytical chemistry* **2011**, *83* (16), 6202-6207.
- Martić, S.; Beheshti, S.; Rains, M. K.; Kraatz, H.-B., *Analyst* **2012**, *137* (9), 2042-2046.
- Kelley, S. O.; Barton, J. K.; Jackson, N. M.; Hill, M. G. *Bioconjugate chemistry* **1997**, *8* (1), 31-37.
- Matharu, Z.; Bhandekar, A. J.; Gupta, V.; Malhotra, B. D., *Chemical Society Reviews* **2012**, *41* (3), 1363-1402.

10. Gasparac, R.; Taft, B. J.; Lapierre-Devlin, M. A.; Lazareck, A. D.; Xu, J. M.; Kelley, S. O. *Journal of the American Chemical Society* **2004**, *126* (39), 12270-12271.
11. Hu, K.; Lan, D.; Li, X.; Zhang, S. *Analytical chemistry* **2008**, *80* (23), 9124-9130.
12. Agüí, L.; Yáñez-Sedeño, P.; Pingarrón, J. M. *Analytica chimica acta* **2008**, *622* (1), 11-47.
13. Daniel, S.; Rao, T. P.; Rao, K. S.; Rani, S. U.; Naidu, G.; Lee, H.-Y.; Kawai, T. *Sensors and Actuators B: Chemical* **2007**, *122* (2), 672-682.
14. Han, J.-H.; Boo, H.; Park, S.; Chung, T. D. *Electrochimica acta* **2006**, *52* (4), 1788-1791.
15. Joo, S.; Park, S.; Chung, T. D.; Kim, H. C. *Analytical Sciences* **2007**, *23* (3), 277-281.
16. Soleymani, L.; Fang, Z.; Sargent, E. H.; Kelley, S. O. *Nature Nanotechnology* **2009**, *4* (12), 844-848.
17. Ding, Y.; Chen, M. *MRS bulletin* **2009**, *34* (08), 569-576.
18. Liu, Z.; Searson, P. C. *The Journal of Physical Chemistry B* **2006**, *110* (9), 4318-4322.
19. Seker, E.; Berdichevsky, Y.; Begley, M. R.; Reed, M. L.; Staley, K. J.; Yarmush, M. L. *Nanotechnology* **2010**, *21* (12), 125504.
20. Xue, Y.; Markmann, J.; Duan, H.; Weissmüller, J.; Huber, P., *Nature communications* **2014**, *5*.
21. Kurtulus, O.; Daggumati, P.; Seker, E. *Nanoscale* **2014**, *6* (12), 7062-7071.
22. Weissmüller, J.; Newman, R. C.; Jin, H.-J.; Hodge, A. M.; Kysar, J. W. *Mrs Bulletin* **2009**, *34* (08), 577-586.
23. Patel, J.; Radhakrishnan, L.; Zhao, B.; Uppalapati, B.; Daniels, R. C.; Ward, K. R.; Collinson, M. M., *Analytical chemistry* **2013**, *85* (23), 11610-11618.
24. Seker, E.; Reed, M. L.; Begley, M. R. *Materials* **2009**, *2* (4), 2188-2215.
25. Seker, E.; Berdichevsky, Y.; Staley, K. J.; Yarmush, M. L. *Advanced healthcare materials* **2012**, *1* (2), 172-176.
26. Yang, Q.; Liang, Y.; Zhou, T.; Shi, G.; Jin, L. *Electrochemistry Communications* **2009**, *11* (4), 893-896.
27. Shulga, O. V.; Zhou, D.; Demchenko, A. V.; Stine, K. J. *Analyst* **2008**, *133* (3), 319-322.
28. Liu, Z.; Du, J.; Qiu, C.; Huang, L.; Ma, H.; Shen, D.; Ding, Y. *Electrochemistry Communications* **2009**, *11* (7), 1365-1368.
29. Zhu, A.; Tian, Y.; Liu, H.; Luo, Y. *Biomaterials* **2009**, *30* (18), 3183-3188.
30. Erlebacher, J.; Aziz, M. J.; Karma, A.; Dimitrov, N.; Sieradzki, K. *Nature* **2001**, *410* (6827), 450-453.
31. Kerman, K.; Ozkan, D.; Kara, P.; Meric, B.; Gooding, J. J.; Ozsoz, M. *Analytica Chimica Acta* **2002**, *462* (1), 39-47.
32. Kara, P.; Kerman, K.; Ozkan, D.; Meric, B.; Erdem, A.; Ozkan, Z.; Ozsoz, M. *Electrochemistry Communications* **2002**, *4* (9), 705-709.
33. Lin, X.-H.; Wu, P.; Chen, W.; Zhang, Y.-F.; Xia, X.-H. *Talanta* **2007**, *72* (2), 468-471.
34. Yang, W.; Ozsoz, M.; Hibbert, D. B.; Gooding, J. J. *Electroanalysis* **2002**, *14* (18), 1299-1302.
35. Gu, J.; Lu, X.; Ju, H. *Electroanalysis* **2002**, *14* (13), 949.
36. Liu, S.-f.; Li, Y.-f.; Li, J.-r.; Jiang, L. *Biosensors and Bioelectronics* **2005**, *21* (5), 789-795.
37. Pan, D.; Zuo, X.; Wan, Y.; Wang, L.; Zhang, J.; Song, S.; Fan, C. *Sensors* **2007**, *7* (11), 2671-2680.
38. Anandan, V.; Yang, X.; Kim, E.; Rao, Y.; Zhang, G. *Journal of biological engineering* **2007**, *1* (1), 5.
39. Scanlon, M. D.; Salaj-Kosla, U.; Belochapkin, S.; MacAodha, D.; Leech, D.; Ding, Y.; Magner, E. *Langmuir* **2011**, *28* (4), 2251-2261.
40. Zhu, L.; Zhao, R.; Wang, K.; Xiang, H.; Shang, Z.; Sun, W. *Sensors* **2008**, *8* (9), 5649-5660.
41. Daggumati, P.; Kurtulus, O.; Chapman, C. A. R.; Dimlioglu, D.; Seker, E. *JoVE (Journal of Visualized Experiments)* **2013**, (77), e50678-e50678.
42. Alligrant, T.M.; Nettleton, E.G.; Crooks, R.M., *Lab on a Chip*, **2013**, *13* (3), 349-354.
43. Xiao, Y.; Lai, R. Y.; Plaxco, K. W. *Nature protocols* **2007**, *2* (11), 2875-2880.
44. Seker, E.; Reed, M. L.; Begley, M. R. *Scripta Materialia* **2009**, *60* (6), 435-438.
45. Tan, Y. H.; Davis, J. A.; Fujikawa, K.; Ganesh, N. V.; Demchenko, A. V.; Stine, K. J. *Journal of materials chemistry* **2012**, *22* (14), 6733-6745.
46. Park, S.; Kim, H. C.; Chung, T. D. *Analyst* **2012**, *137* (17), 3891-3903.
47. Esteban Fernandez de Avila, B.; Watkins, H. M.; Pingarrón, J. M.; Plaxco, K. W.; Palleschi, G.; Ricci, F. *Analytical chemistry* **2013**, *85* (14), 6593-6597.
48. Matharu, Z.; Patel, D.; Gao, Y.; Haque, A.; Zhou, Q.; Revzin, A. *Analytical chemistry* **2014**, *86* (17), 8865-8872.
49. Ricci, F.; Lai, R. Y.; Heeger, A. J.; Plaxco, K. W.; Sumner, J. J., *Langmuir* **2007**, *23* (12), 6827-6834.
50. Huang, L.; Seker, E.; Begley, M.; Utz, M.; Landers, J., Proceedings of the 12th International Conference on Miniaturized Systems for Chemistry and Life Sciences; MicroTAS: San Diego, CA, USA, **2008**; pp 1567-1569.
51. Bin, X.; Sargent, E.H.; Kelley, S.O., *Analytical Chemistry* **2010**, *82* (14), 5928-5931.
52. Das, J.; Kelley, S. O., *Analytical Chemistry* **2013**, *85* (15), 7333-7338.
53. Squires, T. M.; Messinger, R. J.; Manalis, S.R., *Nature biotechnology* **2008**, *26* (4), 417-426.
54. Sheehan, P. E.; Whitman, L. J., *Nano letters* **2005**, *5* (4), 803-807

Table of contents/Abstract figure

